Additive Manufacturing 26 (2019) 180–192

Contents lists available at ScienceDirect

Additive Manufacturing

journal homepage: www.elsevier.com/locate/addma

Heat source management in wire-arc additive manufacturing process for Al-Mg and Al-Si alloys

Kohei Oyama[a], Spyros Diplas[b], Mohammed M'hamdi[b], Anette E. Gunnæs[c], Amin S. Azar[b,*]

[a] Keio University, Department of Mechanical Engineering, Yokohama, Japan
[b] SINTEF Industry, Oslo, Norway
[c] University of Oslo, Department of Physics, Oslo, Norway

ARTICLE INFO

Keywords:
Wire-arc additive manufacturing (WAAM)
Modelling
Aluminium alloys
Wall structure
Robotic cold metal transfer (CMT)

ABSTRACT

Modelling of wire-arc additive manufacturing process is an effective way for adapting the optimum parameters as well as understanding and managing the sequences of layer-by-layer deposition. Some of these parameters such as toolpath, deposition intervals and heat source power play important roles in improving the process viability and cost efficiency. In this article, we have studied Al-5Mg, Al-3Si alloys as demonstrators, from both experimental and modelling perspectives, to benchmark different deposition parameters and provided guidelines for optimising the process conditions. Physical values such as total distortion and residual stress were selected as indicators for the manufacturability of the structure. The simulations were performed by Simufact Welding software, that is outfitted with the MARC solver and the experiments were executed in a robotic cell. We have introduced a method for optimising the process parameters based on the heat source power modification and selection of unique parameters for each deposition layer. This was performed by monitoring the evolution of the molten pool size and geometry when building a wall structure. The results suggest that achieving an uninterrupted deposition process entails modification of the heat input for each layer. Thus, a simple analytical method was proposed to estimate the heat input reduction coefficient for a wall structure as a function of molten pool geometry and the height at which, a new layer is being deposited. It was also shown that a generic selection of parameters for aluminium alloys may impair the eventual quality for some of the alloys due to their inherent physical properties such as high temperature flowability.

1. Introduction

Additive manufacturing (AM) is rapidly turning into one of the major processing mainstreams for metallic components [1]. Among all AM methods, wire-arc additive manufacturing (WAAM) is accentuated [2] because of its two major competitive advantages: *i)* The deposition rate and consequently, production efficiency and profitability of WAAM are among the highest in AM methods [3]. Although the method is challenged in terms of the structural complexity (e.g. lattice structure etc.) and metrological precision [4], it can still be favourable for deposition of large near-net shape structures, even though it consumes reasonable time and resources [5]. *ii)* The original physical process in WAAM is welding and joining of metals, which encompasses decades of accumulated knowledge and advanced instrumentation for the industrial and research community [6].

In terms of advanced equipment, one of the significant contributions in the recent years is associated with the cold metal transfer (CMT) method. Invented by Fronius in mid-2000's, CMT reduced the processing heat input by cycling the arcing and short-circuiting phases at a relatively high frequency [7,8]. Pickin and Young [9] compared the conventional joining methods such as gas metal arc welding GMAW and P-GMAW (pulsed variant) with CMT on Al-alloys and concluded that the deposition efficiency and control of penetration (dilution) is superior in the CMT method. Depending on the settings, the depth of penetration can be so low that the method is preferred in low-dilution cladding [10]. It was also reported for Al, that alternating processes such as CMT and P-GMAW efficiently remove the tenacious surface oxide and bring a more mechanically robust deposition about [11–13]. Several researchers used CMT as a method of choice for several different materials such as Ti-6Al-4V [14], Al alloys [15–19], AZ31 Mg alloy [20] and steels [21–23].

Nevertheless, as a natural entrance to the field, and due to lack of suitable modelling approaches for early researchers, most of the process optimisation were through tedious and costly experimental trial and

* Corresponding author at: SINTEF Industry, Forskningsveien 1, 0373, Oslo, Norway.
E-mail address: amin.azar@sintef.no (A.S. Azar).

https://doi.org/10.1016/j.addma.2019.01.007
Received 27 September 2018; Received in revised form 30 December 2018; Accepted 23 January 2019
Available online 30 January 2019

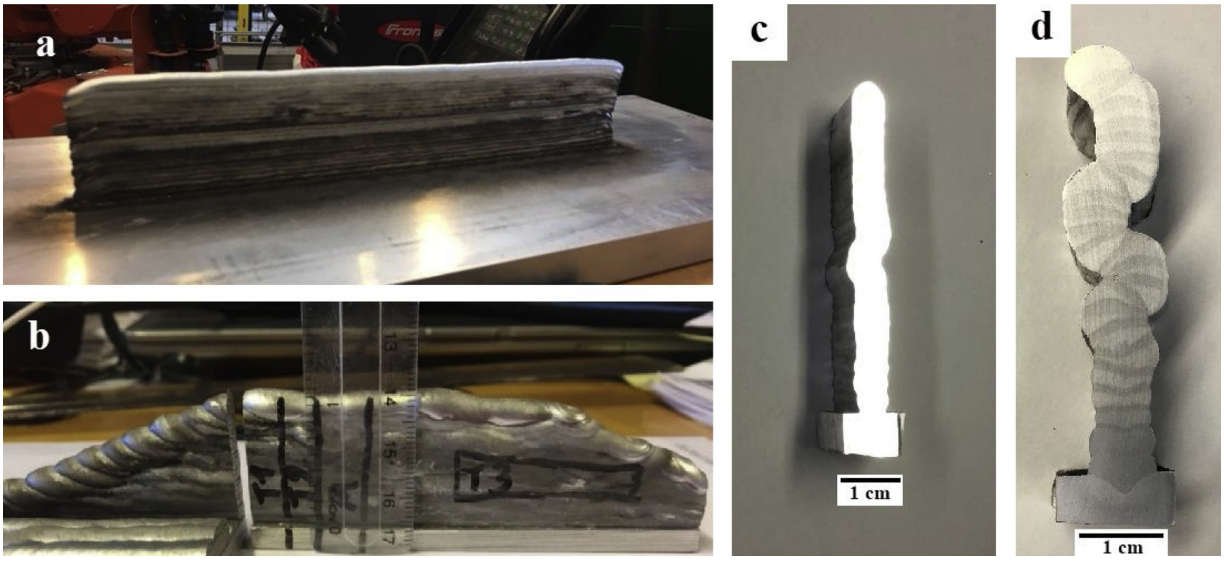

Fig. 1. Wall structures made from (a) Al-5Mg and (b) Al-3Si. The walls are almost 20 cm long. Cross section of the deposited wall structures using (c) Al-5Mg and (d) Al-3Si.

error processes. Adapting the toolpath for the given constant layer height and bead width values undermines the fact that the material will undergo a thermal cycle with different cooling conditions, depending on the geometry of the deposited material. Therefore, detailed modelling work is required to increase the understanding of the effect of certain parameters used in the WAAM process. Ding's work [24] on thermo-mechanical finite element simulation of the WAAM was among the early comprehensive contributions in the field. Ding et al. [25] applied a moving heat source on a high aspect ratio structure to observe the thermally induced stresses and distortion. Although they reported a good agreement between the measured and calculated results, the model has two major vulnerabilities: *i)* The whole structure, which is the geometry after completion of the deposition, was present from the beginning of the process and boundary conditions were applied constantly on the entire structure. This is far from the real case scenario, where the boundary conditions are applied gradually only on the deposited material. *ii)* The model was not optimised for the solver and the entire calculation took very long in terms of the elapsed wall-clock time. This makes the whole model unusable for benchmarking studies and conventional trial and error will still be more efficient for establishing the optimum parameters. Denlinger et al. [26] presented some methods aiming to reduce the simulation time. They achieved one step of improvement in their model in terms of the applied boundary conditions. In their model, each layer appeared when deposited and they subsequently applied the boundary conditions upon its appearance (quiet inactive element approach). Although, this approach may result in better accuracy, it is still far from what happens in practice, where each element should appear along the deposition path. According to their conclusions, they managed to reduce the simulation time significantly, however, the predicted values showed large deviation from the experimental measurements. Montevecchi et al. [27] illustrated finite element simulations of a low-height wall structure using the single element activation approach at the vicinity of the heat source. They also proposed a new heat source model and showed that the experimental and modelling results were in close agreement because of their choice of method.

The abovementioned studies tried to show that the utilised specific finite element model (FEM) might have worked better than others' in a certain setting. The next step in putting the FEM knowledge into practice would be to use them in benchmarking cases and optimise the process parameters by studying the "digital twin" [28,29] model of a real case. Distortion has been mainly used in most of previous studies as a performance- or manufacturability-indicator, but there are nevertheless more challenges to be considered in the WAAM process. For instance, residual stresses, metrological and geometrical accuracy, temperature dependent mechanical and physical properties, heat flow fields, defects and anomalies and in case of wall structure, anisotropy and sagging on the side are among the major challenges.

In order to improve our insight about the process parameters and their role on the challenges, we introduced a procedure for managing the heat source, by modifying its energy density during the process. Wall geometry simulation cases were created identical to the experimental trials followed by systematic variations of process parameters to observe their effect on the mechanical performance and metrological tolerances. The study is focused on two Al alloys, namely Al-5Mg and Al-3Si. The simulation results were compared with experimental measurements to demonstrate the benefit of the modelling approach. In addition, a layer-by-layer heat source modification approach was introduced as a simple mathematical tool to abate any complexity for industrial uptake. This approach underlines the importance of the material and process parameter selection, aiming to compensate for some of the structural and metrological defects in the wall structure.

2. Experimental procedure

2.1. Structure and materials

Wall structures were constructed by WAAM in a robotic cell, equipped with ABB-IRB 2400 robot and TPSi-400 CMT power supply unit. Two different Al alloys were deposited; Al-5Mg, and Al-3Si as shown in Fig. 1(a) and (b) respectively. In both cases, a 200 mm wall was deposited on a substrate with dimensions of 300 × 150 × 20 mm. The chemical compositions of the materials are given in Table 1. The experimentally determined processing parameters for each alloy are tabulated in Table 2. In this table, U, I, V and η stand for open circuit voltage, arc current, travel speed and process efficiency, respectively. Since the deposition sequence was in semi-automatic mode, the interval between deposition of two adjacent beads was scheduled to be long enough so that the onset of each deposition step could be confidently assumed at a low temperature. However, the interval parameter was among the ones that are tested for different values in the finite element simulations. The substrate was extracted from a wrought 6160 slab of aluminium alloy.

Table 1
Chemical composition of the materials in wt%.

Material	Si	Fe	Cu	Mn	Mg	Ti	Be	Others	Al
Al-5Mg	≤0.2	≤0.4	≤0.1	0.5-1	4.3-5.2	≤0.15	≤0.0008	0.15	Rest
Al-3Si	2.5-3.5	≤0.20	≤0.30	0.8-1.2	≤0.01	≤0.005	≤0.0003	≤0.02	Rest

Table 2
Experimental process parameters for the wall structure.

Material	U [V]	I [A]	V [mm/s]	η [-]
Al-5Mg	15.2	156	8	0.9
Al-3Si (First layer)	15.3	177	6	0.9
Al-3Si (Subsequent)	18.0	115	6	0.9

2.2. X-ray measurements and metallography

After fabricating the wall structure, the residual stresses of the Al-3Si alloy were measured using x-ray diffraction (XRD). The measured points on the wall and the substrate are illustrated in Fig. 2. For complementary metallographic analysis and improving the probe head accessibility, the sample was cut close to the middle of the wall and the XRD measurements were taken from one half of the whole structure. In this context, it was assumed that the evolution of stresses will have a two-plane symmetry; longitudinal and transverse planes in the middle of the wall. Moreover, the XRD measurements were performed at regions away from the cut surfaces to eliminate stress relaxation effects. The closest set of measured points was 88 mm far from the cut edge. Fig. 3(a) shows the experimental XRD measurement setup. The x-ray probe was placed over each indicated measurement point and rotated within $2\theta = 123^{\circ}$ to 171° for the characteristic peak search. By collecting diffraction data in two different angles, as shown in Fig. 3(b), residual stress can be measured. Fig. 3(b) also shows the principles of x-ray residual stress measurement. In this figure, ψ is the incident angle and α is the reflective angle. The following formulation was utilized to calculate the residual stress, σ [30];

$$\sigma = K(2\alpha_1 - 2\alpha_2) \tag{1}$$

$$K = \frac{E}{1+\nu} \tag{2}$$

where K is bulk modulus, E is Young's modulus and ν is Poisson's ratio.

3. Modelling procedure

3.1. Deposition geometry and boundary conditions

In order to identify the optimum process parameters, a series of systematic simulation cases were prepared, considering only the wall structure. The constructed model including the free-body illustration and the boundary conditions are shown in Fig. 4. For the finite element analysis, *Simufact Welding* software was used. The sizes of the base plate and the beads were provided in Table 3. 22 beads were deposited on the middle of the substrate, replicating the experimental conditions. In order to obtain data from specific regions, data recording points were embedded on the nodes across the wall height and substrate width, and shown as wall-middle, wall-edge, base-middle and base-top in Fig. 4. The deposition sequences and intervals are defined in separate cases as it will be shown later in Section 3.3. Imitating the experimental conditions, the substrate was placed on a work bench (called bearing in the simulation) and four clamps were used to fasten the substrate on the bearing. The centre of each clamping cylinder was placed 20 mm away from the edges of the base plate. Both the depth and radius of these clamps were 10 mm. The size of the bearing was fitted to the substrate except for the depth, 10 mm. The clamps are required to prevent movements and angular distortion of the plate when deposition is in progress. The temperature was set to 20 °C (room temperature) at the onset of the simulations. The temperature of each quiet element was set to the melting point of that specific material upon appearance with the heat source position.

3.2. Material models

The material used for the substrate and the bearing was TL-10014 (an Al-alloy with composition and mechanical performance between 6016 and 6082 in T4 condition). The investigated deposition materials were Al-5Mg and Al-1Si. The chemical composition and properties of Al-1Si are close to those of Al-3Si and therefore this material was substituted from the calibrated data library in the software. Temperature dependent physical and mechanical properties of these materials are presented in Figs. 5 and 6.

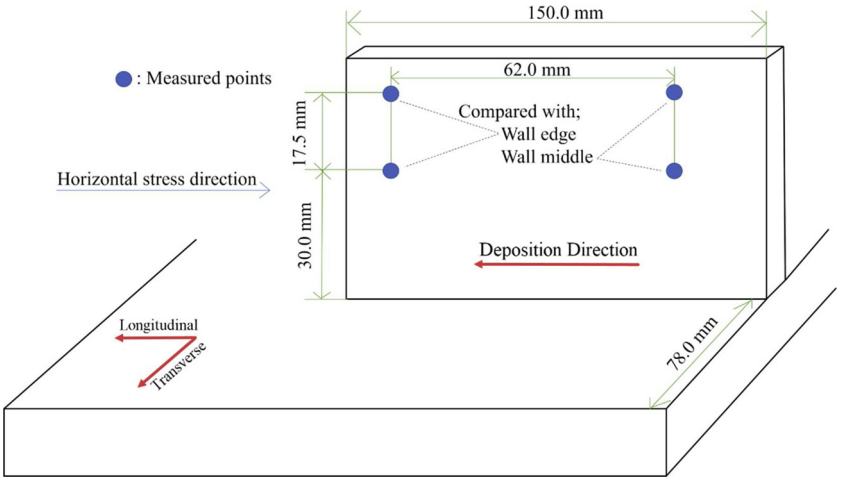

Fig. 2. X-ray measurement points on Al-3Si.

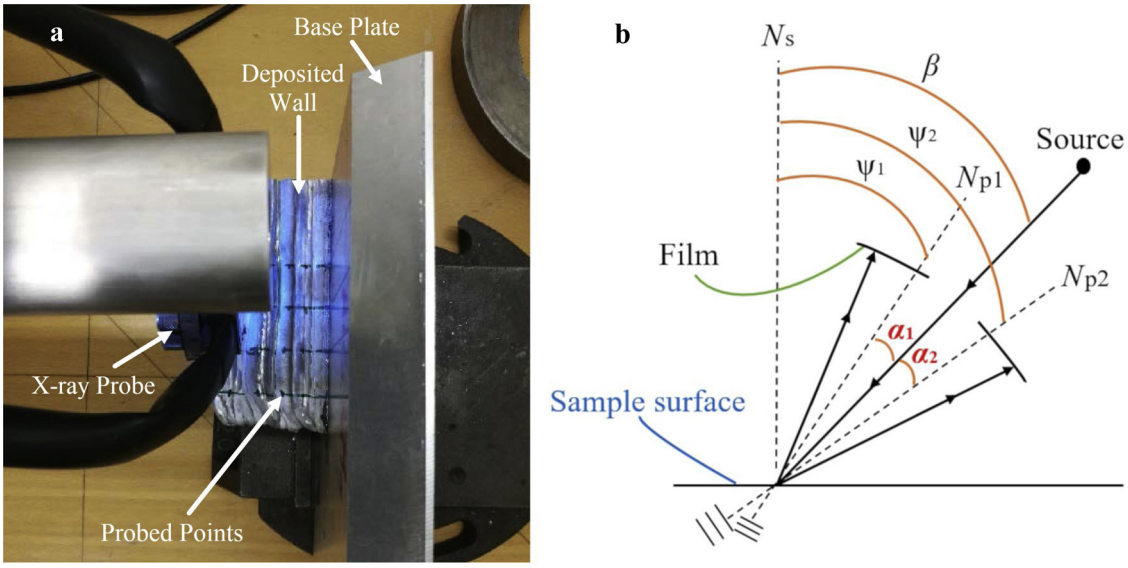

Fig. 3. (a) X-ray measurement setup and (b) Schematic illustration of x-ray residual stress measurement principles.

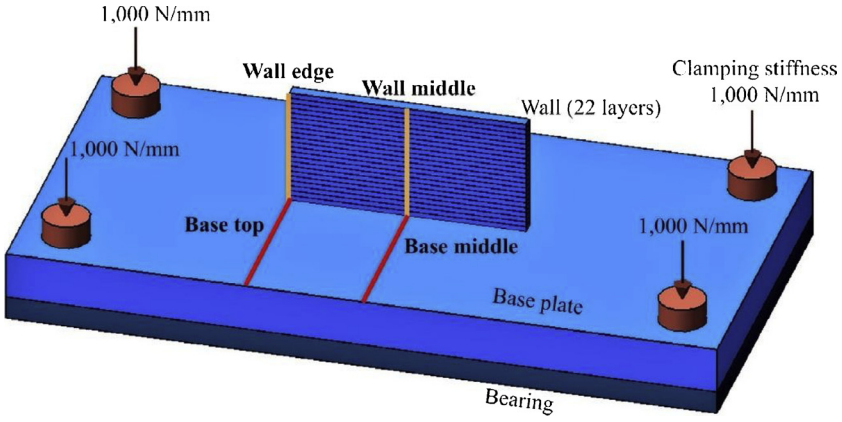

Fig. 4. Model construction with applied boundary conditions and data recording lines.

Table 3
The sizes of components.

	Length [mm]	Width [mm]	Depth [mm]
Base plate	300	150	20
Bead	100	5	2.28

3.3. Modelled cases

The deposition parameters in each simulation case were applied according to Table 4:, following the experimentally determined values. In some of the cases, the parameters were modified to reach a certain objective as it will be discussed later. Using the Al-5Mg material, in case 1, the beads were deposited along a single direction from edge to edge without any intervals between each two overlying beads (no interval can only be achieved using multiple deposition sources. Otherwise, the robot arm compels a few seconds to resume to the home position). In case 1-M ("M" stands for modified), the heat source modification was applied. a_i and b_i were used as heat source modification coefficients that are going to be scrutinised in the results section. In case 1-I ("I" stands for inversed interlacing), the deposition direction was reversed at every layer. The deposition was still without intervals. In case 2, the intervals between each process were set to 120 s, and the deposition direction was not reversed, similarly to case 1. Al-1Si was applied to case 3 in which, the process direction and intervals were the same as case 2. Similar to the experimental conditions, this will set an inter-layer deposition temperature below 120 °C.

A double ellipsoid moving heat source [31] was considered in the simulations as illustrated in Fig. 7(a) and (b). The double ellipsoid heat source parameters are given in Table 5, following the heat source geometry determination routine given in [32]. The elements are distinguished as two kinds: quiet (inactive) and active. The quiet elements appear and remain active during the deposition when the heat source is present at that very location. The initial temperature of the appearing elements is set to the melting point for that specific alloy. Thereafter, the appeared elements will be exposed to the heat source power, and the temperature may rise beyond the heat source position owing to heat conduction.

As an initial step, the simulation cases 1, 2 and 3 were performed. Later, based on the results from these cases, a few complementary cases were defined in which, some parameters were studied. The original size of the mesh elements on the wall structure was 2 mm. The mesh size was kept identical for all the simulation cases since the objective of this study was benchmarking a few cases. The simulation results as well as a method for heat source management are presented in the next section.

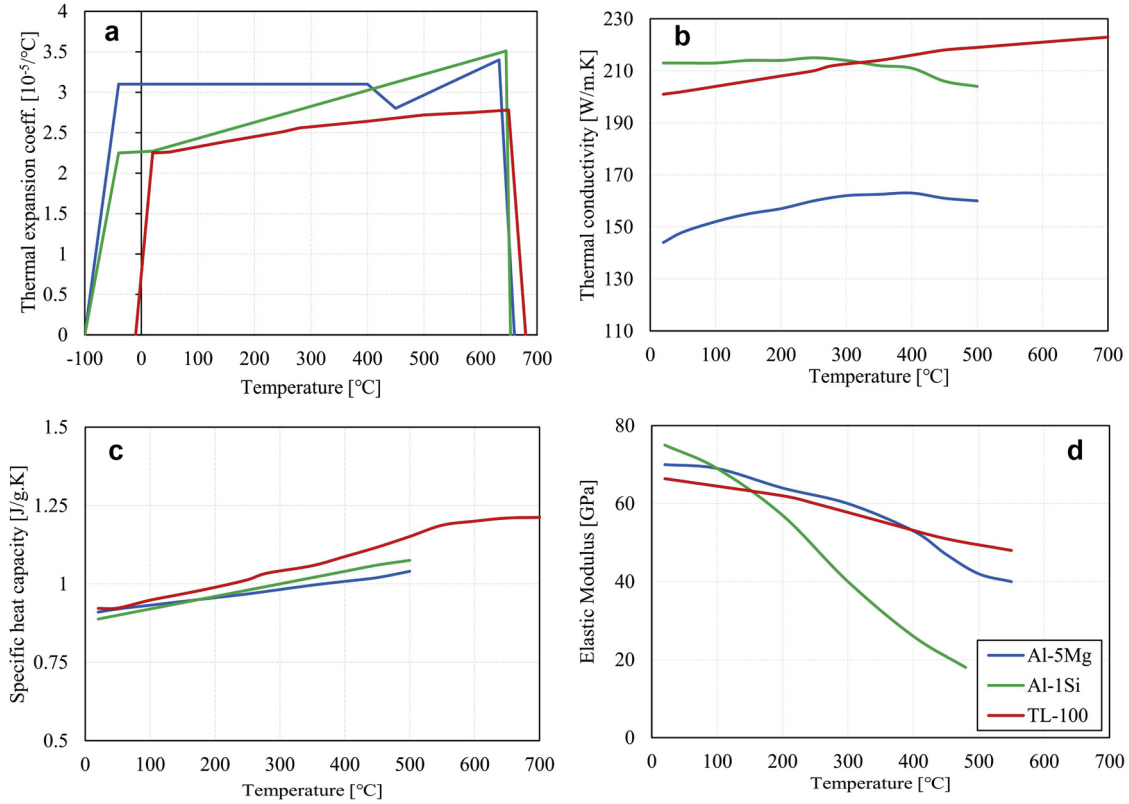

Fig. 5. Physical properties of Al-5Mg, Al-1Si and TL-100 (a) thermal expansion coefficient (b) thermal conductivity (c) specific heat capacity and (d) temperature dependent elastic modulus.

4. Results and discussion

4.1. Cases using Al-5Mg

As described earlier, the experimental process was paused between deposition sequences of each two adjacent beads. This makes deposition longer and any idle time will result in low process productivity. Therefore, the goal is to have a process that runs continuously without any imposed idle time. During manufacturing of a relatively large component, the already deposited material will be given enough time to cool down to an acceptable level prior to the deposition of the next layer. However, continuous deposition may increase the overall temperature of the component and impose excessive material flow. Therefore, we consider case 1 as representative of continuous deposition in order to investigate the process viability. Fig. 8 illustrates the development of the molten metal region. It was observed that the molten pool became excessively broad as the newly deposited beads were getting distant from the base material (i.e. the wall was becoming higher). Large molten pool implies that the manufacturability of the wall geometry is impaired due to the increased chance for molten metal flow, and the structure cannot be processed using a continuous deposition strategy under the given process parameters.

The excessive molten pool size cannot exist in the experimental practices. Instead, the deposited material will flow, and the wall structure will sag. In the numerical model, we have introduced a non-zero flow stress values for temperatures above the melding point in order to prevent excessive mesh element distortions.

As an attempt to mitigate the observed problem, case 2 was defined, where an idle period of 120 s was set in between two consecutive layers to allow the structure to cool down. Montevecchi et al. [33] also observed the above demonstrated molten pool size growth. This was the major motivation for their finite element studies and they proposed an

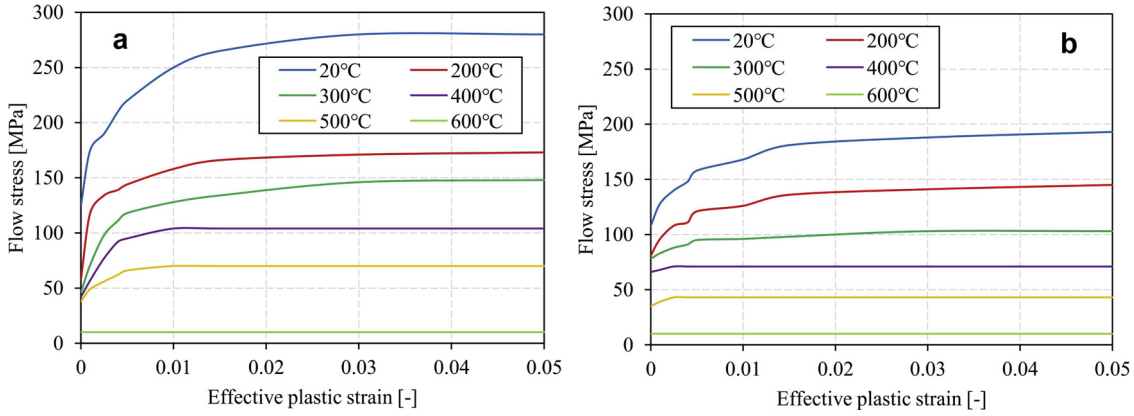

Fig. 6. Temperature dependent flow curves for (a) Al-5Mg and (b) Al-1Si alloys.

Table 4
Conditions of cases. "M" stands for modified heat source and "I" stands for inversed interlacing. U is voltage, I is current, V is travel speed and η is the process efficiency.

Case	*Deposited Material*	*Heat source parameters from base to top*	U [V]	I [A]	V [mm/s]	η [-]	Intervals [s]
1	Al-5Mg	Constant	15.2	156	8	0.9	0
1-M	Al-5Mg	Modified	15.2	156	8	$0.9a_i$	0
1-I	Al-5Mg	Constant	15.2	156	8	0.9	0
1-IM	Al-5Mg	Modified	15.2	156	8	$0.9a_i$	0
2	Al-5Mg	Constant	15.2	156	8	0.9	120
2-M	Al-5Mg	Modified	15.2	156	8	$0.9b_i$	120
3 (First layer)	Al-1Si	Constant	15.3	177	6	0.9	120
3 (Subsequent)	Al-1Si	Constant	18.0	115	6	0.9	120

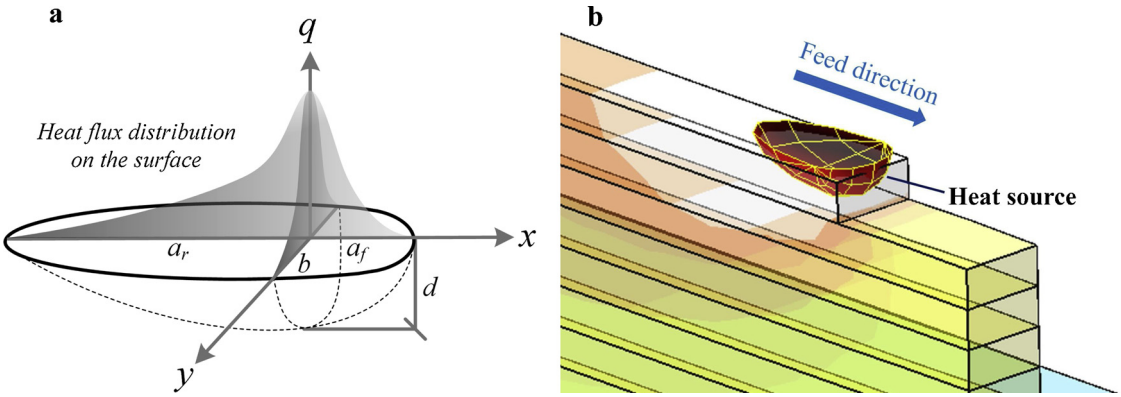

Fig. 7. (a) Illustration of double ellipsoidal volume heat source parameters and (b) moving heat source and mesh element activation approach in the simulations.

Table 5
Double ellipsoid volume Gaussian heat source parameters.

a_f [mm]	a_r [mm]	b [mm]	d [mm]	Gaussian parameter	Heat front scaling factor
2.0	7.0	2.5	2.3	3	0.444

algorithm based on which, the idle time can be minimised between each two deposition layers. In the present study, the idle time was constantly maintained at 120 s between each layer. According to our simulations (see Fig. 9), the temperature of the deposited material was sinking below 120 °C in the given time as required for inter-pass temperature by the manufacturer of the deposition wire material. Fig. 9 shows, the molten metal region is not as broad as it was in case 1. However, the size of the pool is still very large, extending over more than 4 subsequent layers at higher deposition heights.

Although the idle time improves the viability of the process, the overall molten pool size is still beyond rational limits. Despite starting each layer from relatively lower temperature compared to the continuous deposition case, the molten pool size is still on the growth regime. Moreover, idle time is counterproductive since it makes the process slow and less profitable.

When material is deposited at lower layers, the heat source is close to the substrate and the heat can flow throughout the substrate. However, when the deposition layer is far from the substrate, the heat can only flow through the previously deposited geometry and therefore, the heat dissipation is not as effective as it is for the lower layers. This results in accumulation of heat in the deposited structure and gradual increase of the baseline temperature. In other words, the idle time will affect positively the process viability only to a certain extent and especially for low wall geometries or wall geometries at an early deposition stage, where the small amount of the deposited material will enable fast heat flow towards the substrate.

In order to provide a solution for this challenge, a method for modifying the heat source was introduced. In this method, the depths of

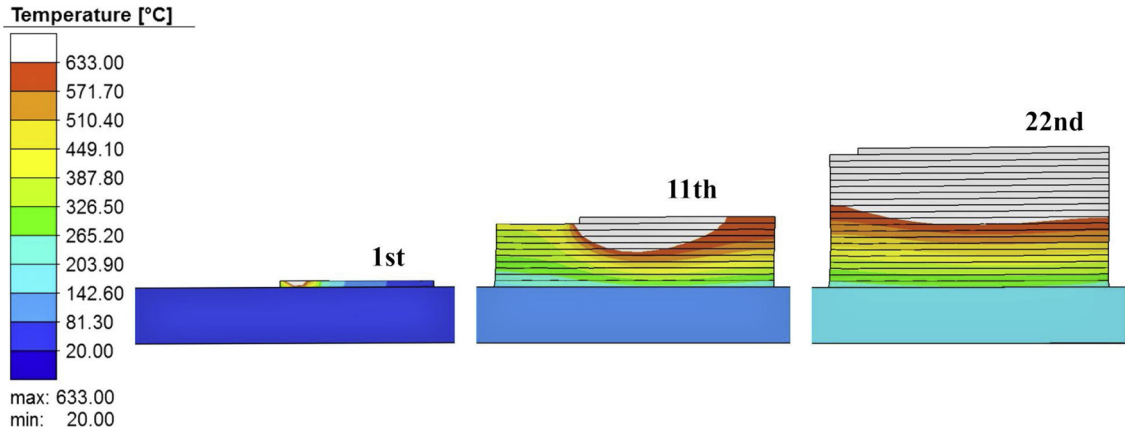

Fig. 8. Molten region size of case 1, showing the evolution of the region as the wall was becoming higher.

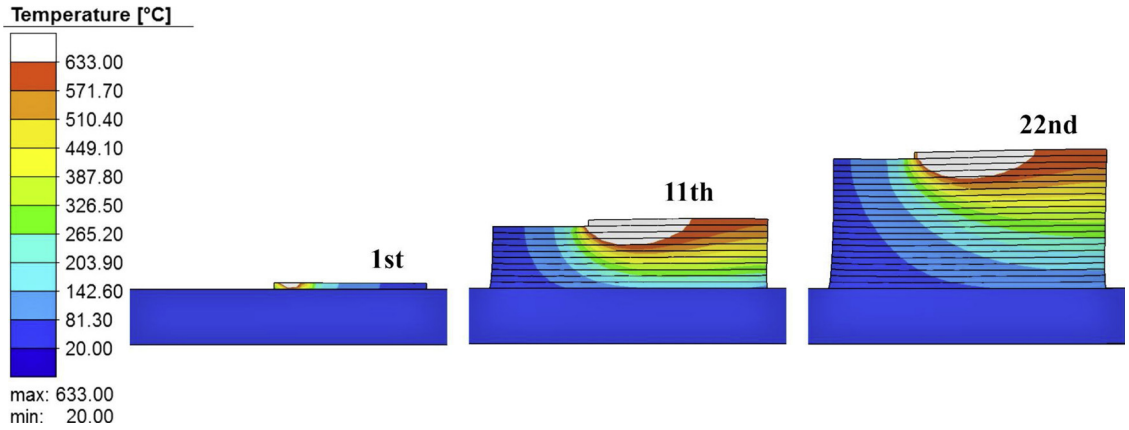

Fig. 9. Molten region size of case 2, showing the evolution of the region after introducing 120 s of idle time between two adjacent layers.

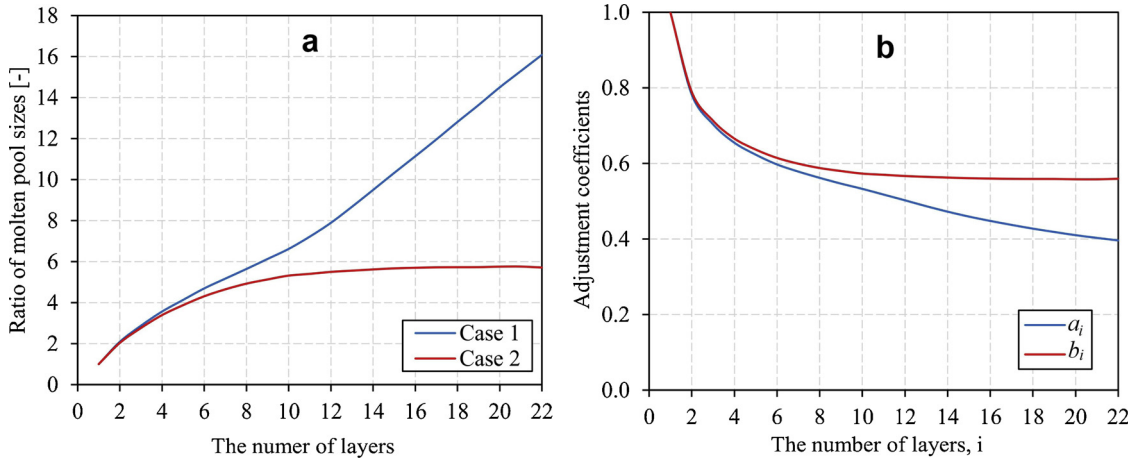

Fig. 10. (a) Ratio between depths of molten pools in the first layer and in each layer, (b) 22 values for adjusting heat source acquired from simulations.

the molten pool size in case 1 and case 2 were recorded. Fig. 10(a) shows the ratio of the molten pool depth at each layer over the pool depth after deposition of the first layer for case 1 and 2. The ratio was calculated based on the following equation:

$$(Ratio)_i = \frac{Depth\ of\ the\ molten\ pool\ at\ the\ i^{th}\ layer}{Depth\ of\ the\ molten\ pool\ at\ the\ 1^{st}\ layer} \tag{3}$$

It can be seen that the molten pool size increases monotonically for case 1. For case 2, the molten pool size increases until it reaches a stable plateau. This implies that the programmed idle time of 120 s helped the molten pool size to remain stable at about 6 times the molten pool size of the first deposition layer. As a solution, a correction value (adjustment coefficient) was determined as a multiplier to the process efficiency factor based on the rate of the molten pool growth and this factor was applied in each new layer. Since the heat source has a volumetric geometry and heat is conducted in all three Cartesian axes, the adjustment coefficient was obtained as the inverse of the cubic root of the molten pool variation in the depth direction based on the following equation:

$$a_i\ or\ b_i = \frac{1}{\sqrt[3]{(Ratio)_i}} \tag{4}$$

Fig. 10(b) shows the calculated adjustment coefficient for each of the 22 deposition layers. The adjustment coefficient for case 2 shows the same plateau as it was described earlier, implying that no further heat source modification is required after about layer 12. However, since the ratio for case 1 does not stabilise by the end of the last layer, the adjustment coefficient will decrease accordingly.

The calculated values can now be used as a coefficient to the process efficiency in this simulation as shown in the following equation:

$$(Heat\ input)_i = (Adjustment\ coefficient)_i \times \eta\frac{UI}{V} \tag{5}$$

where η is the arc efficiency, U is the arc voltage, I is the arc current and V is the heat source travel speed. Multiplying the adjustment factor to any of the process parameters will theoretically affect the process in the same manner. However, in real practice, the coefficient should be applied to either of the process parameters (i.e. U, I, V, η) or a combination of them as long as the arc maintains its relative stability and the modified parameters fall within the sustainable process window. Zhu et al. [34] applied a similar correction factor to the laser metal deposition (LMD) system. However, they used the molten pool temperature distribution as an adjustment reference in contrast to this study, where the pool geometry is used instead.

Fig. 11 shows the simulation results under the case 1 conditions after applying the heat source modification factor. This case is represented as case 1-M as discussed earlier. It is obvious that the molten pool size is the most stable among the previously demonstrated cases (e.g. cases 1 and 2).

The presented cases are for the scenarios where all the layers are deposited along the same direction. In the real case scenario, the robot should move the deposition head from the finish point of the previous layer to the start point of the new layer and that enforces an idle time. The length of the pause depends on the size of the structure: the larger the sample, the longer the distance for the robot to travel. The cumulative idle time for each component may range from several minutes to even hours. In order to increase the productivity beyond the modified case, the heat source modification was applied to a case where the

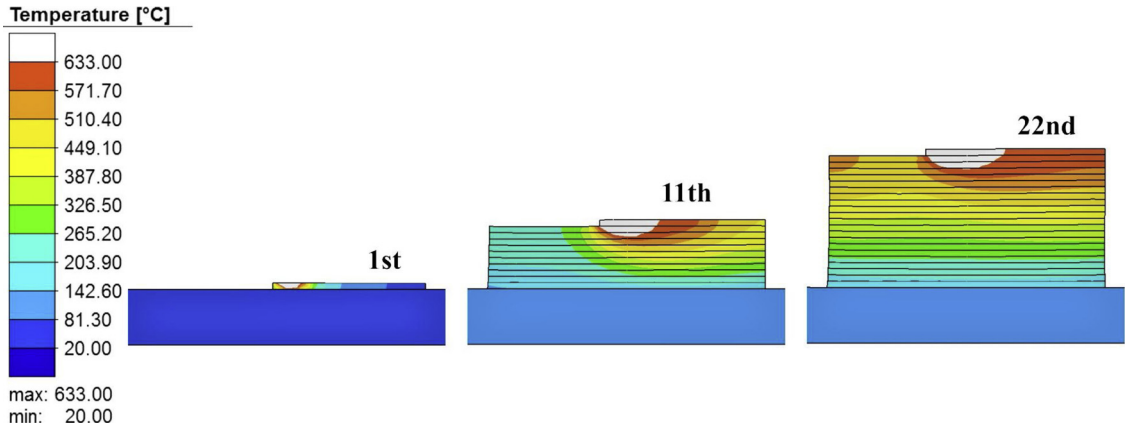

Fig. 11. Molten pool size evolution in case 1-M.

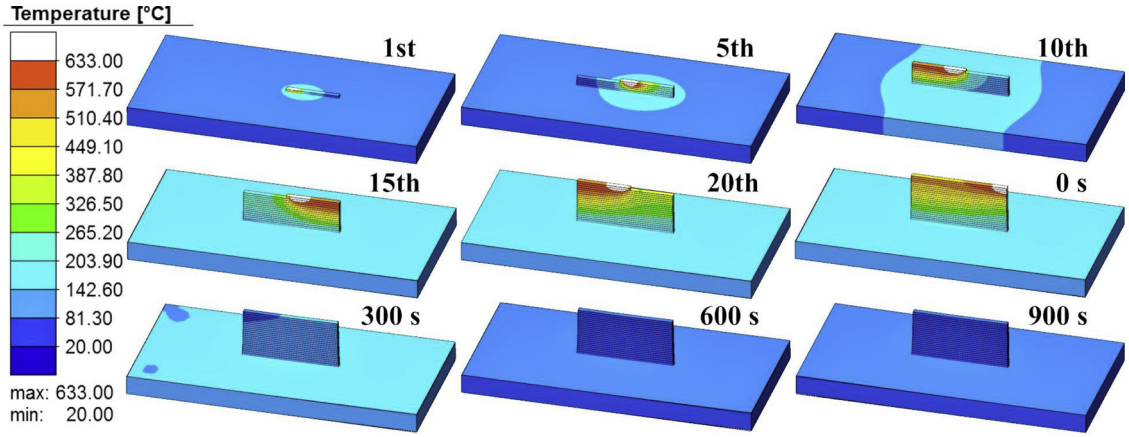

Fig. 12. Temperature field for case 1-IM. The figure shows evolution of the molten pool size for selected deposition layer followed by 900 s of cooling time after the deposition phase.

deposition path is reversed at every layer, mimicking a non-stop deposition of the material. This case is named "interlacing deposition" and the "I" annotation was used after the simulation case number. Fig. 12 shows the temperature field results for the interlacing case 1-IM. As it can be seen, the molten pool size is quite stable throughout the process and the heat source modification is an effective way towards molten pool size stabilization, especially for the continuous deposition regime.

So far, the heat source modification approach was applied regardless of the other influential factors for this type of processing. Parameters such as residual stresses and distortions will also affect the structural integrity of the eventual wall structure. Figs. 13–15 illustrates the effective (von Mises) stress fields for cases 1-M, 2-M and 1-IM respectively. It should be noted that the scale bars of stress simulations were equalised for the sake of case-by-case comparison. Hence, the maxima and minima on the legend may not be from the reported frame. The lower right-hand side frames show the effective stress fields after cooling to room temperature in the reported cases. The distribution and magnitude of the effective stresses seem to be similar in all cases, justifying that the heat source modification increases the manufacturability of the wall structure regardless of the toolpath. In other words, if

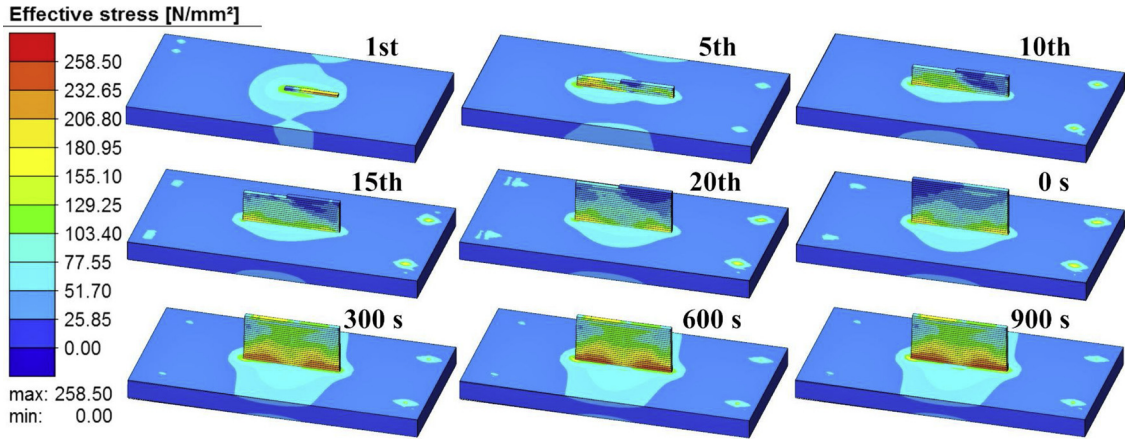

Fig. 13. Effective stress of case 1-M.

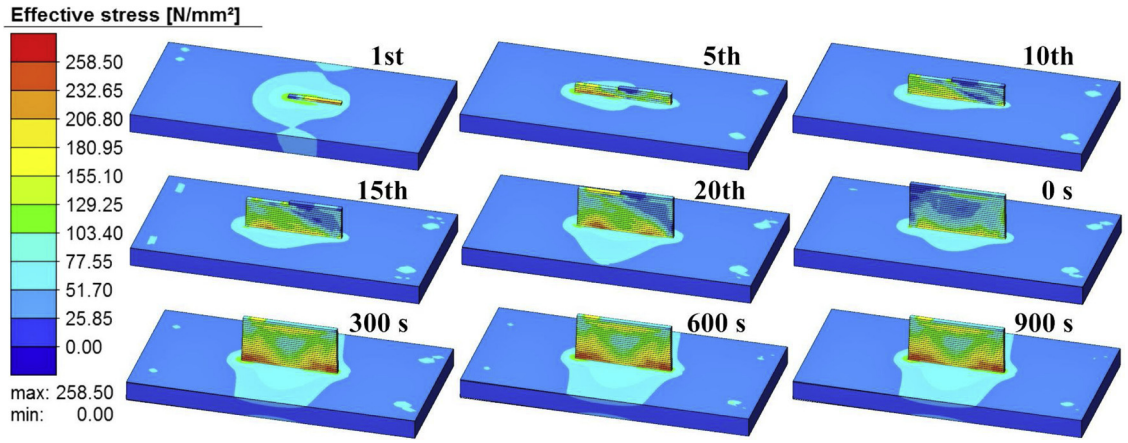

Fig. 14. Effective stress of case 2-M.

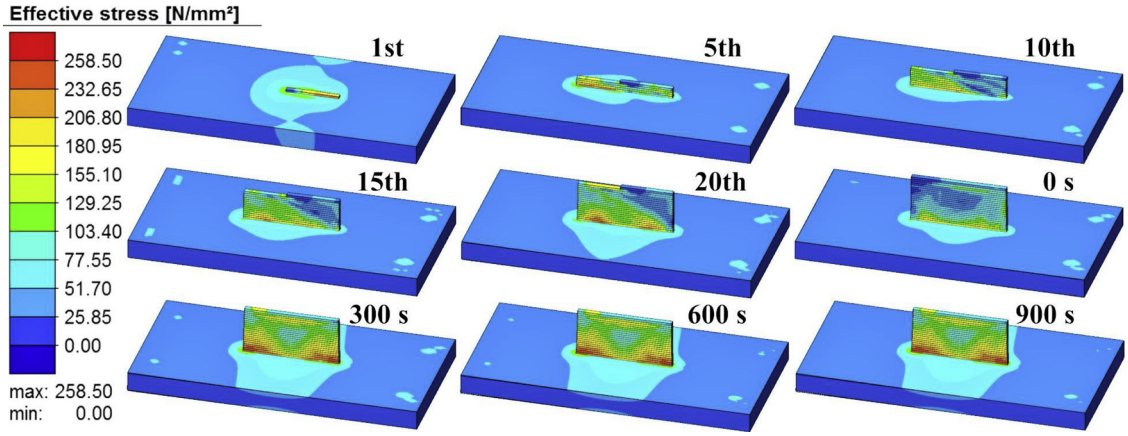

Fig. 15. Effective stress of case 1-IM.

the heat source is adjusted for each deposition layer, most productive deposition toolpaths can be selected, as they will result in similar evolution of stresses.

Fig. 16 summarises the distribution of the effective stress and z-distortion (warpage) on the substrate from the toe of the wall to the edge of the base plate, at the end of the simulation (i.e. cooled to room temperature). The path where these data were taken are illustrated as "base top" and "base middle" in Fig. 4. The stress and distortion values are reported for the simulation cases before and after implementation of the heat source modification. The solid and dashed lines are representing the results for cases from before and after heat source adjustment respectively. Although deposition of the wall structure without heat source power adjustment was shown to be impractical and the amount of cumulative heat input is different, the results from the substrate were taken to show that there are minute differences in the stress values. The stresses on the substrate, in the regions close to the middle and top of the wall, seem to evolve differently in all presented cases. However, the case-by-case values are still comparable. Despite minute differences in the evolved stresses, the z-distortions are different when the heat source is modified, and the deposition strategy is changed. The notable variation of the z-distortion in all the cases are from the region of the substrate that is close to the top of the wall (c.f. Fig. 4).

For instance, modifying the heat source in case 1 results in higher z-distortion on the region close to the top of the wall. On the contrary, lower z-distortion is observed in case 1-I and almost no change was detected in case 2 after heat source modification.

Case 1-IM shows the lowest distortion on the substrate close to the top of the wall among all cases. The latter observation is yet another indication that continuous deposition in the interlacing toolpath regime using heat source modification will benefit the structural integrity by limiting the z-distortion, in addition to the previously presented productivity improvements.

The z-displacement results on the substrate from case 2 and case 2-M are very close in regions close to the top and middle of the wall structure. In terms of metrological accuracy, this is probably the most preferred approach, as there is almost no longitudinal warpage on the substrate. On the other hand, since the warpage on the substrate results in longitudinally distorted wall structure, little difference between wall top and wall middle is representative of a straight geometry with flat bead surface, which is beneficial for the deposition of many subsequent layers.

4.2. Case using Al-1Si

According to Fig. 6, the flow stress of the Al-1Si composition are lower than for Al-5Mg alloy at elevated temperatures. This means that the former material will be prone to deformation during the deposition and it is important to manage the toolpath and the heat source modification in order to achieve an efficient manufacturability for the material.

Fig. 17 shows the temperature field during deposition and cooling phases. The applied process parameters cause excessive molten pool size.

Fig. 18 shows the distribution of the effective stresses during the deposition and after the dictated cooling phase. Compared to the results from case 1-M, 2-M and 1-IM, the level of stresses close to the toe of the wall is somewhat lower when using Al-1Si material. However, the

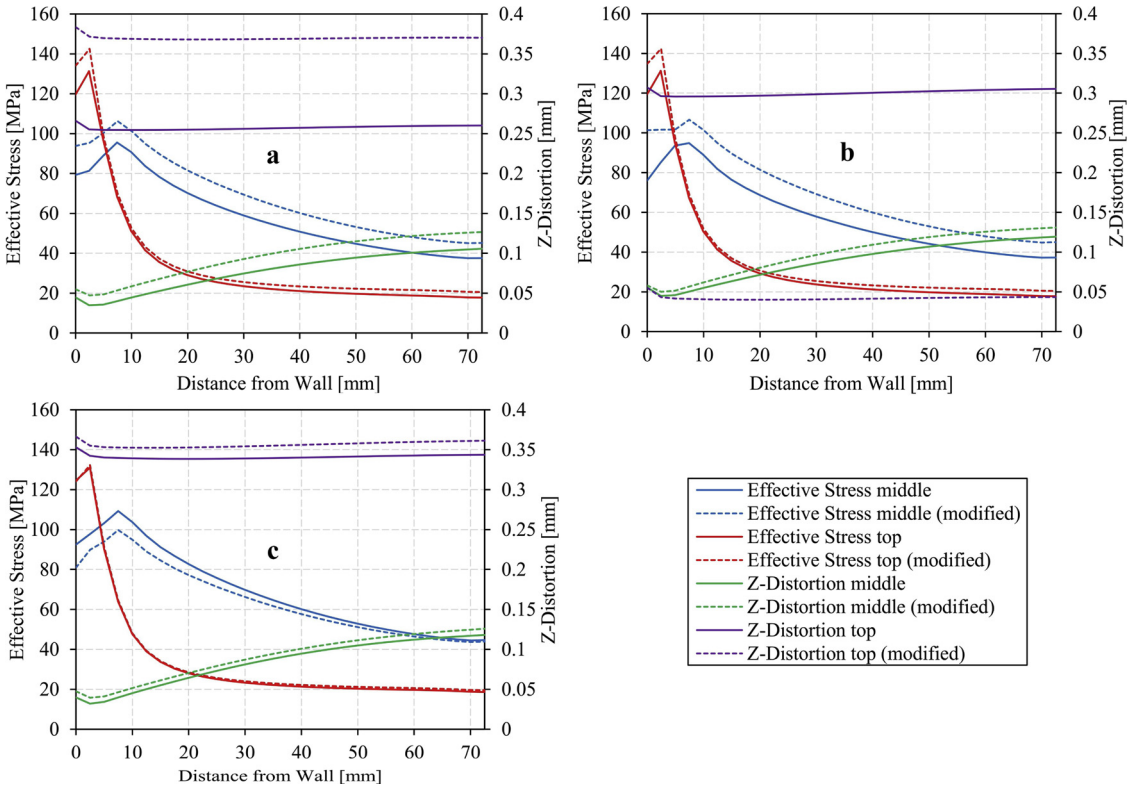

Fig. 16. Effective stress and Z-distortion of the substrate from.
(a) case 1 & case 1-M (b) case 1-I & case 1-IM (c) case 2 & case 2-M.

major difference is the observed excessive deformation on the wall structure. Fig. 19 shows the total displacement on the body of the structure. Apart from deformation on the edges of the wall, the surface of the last layer is uneven, meaning that the pre-programmed toolpath may fail depositing the layers consecutively.

Fig. 20 shows the total displacement field for a some of the cases in this study. The minimum and maximum values were normalised for the presented cases to visualise the difference in the distribution of the displacement for each given deposition conditions and materials. The interlacing cases show a symmetric distribution of the stresses while the cases with unidirectional deposition path are rather asymmetric. Case 2 is showing the highest displacement among others.

The excessive distortion phenomenon and wall sagging was also observed in the experimental conditions for this material. Fig. 1 (c, d) compare the extent of distortions from the cross section of the Al-5Mg and Al-3Si deposited walls. In both experimental cases, no heat source modification was applied and therefore, the wall geometries are the result of parameters implemented in cases 2 and 3 respectively.

Following the earlier descriptions, the resulting metrological deviations in the wall structure can be directly related to the material properties and imperfect selection of the process parameters. As depicted in Fig. 1(d), a few early layers were deposited on top of each other without significant sagging or deviation from the designed wall geometry. This is because of efficient heat dissipation through the substrate causing relatively fast cooling rate for the deposited material at the initial deposition stages. Referring to the simulation results in Fig. 19, it can also be observed that the excessive deformation takes place at higher layers, confirming that the heat source modification is required along the build direction, especially for the materials that have low flow stresses at elevated temperatures.

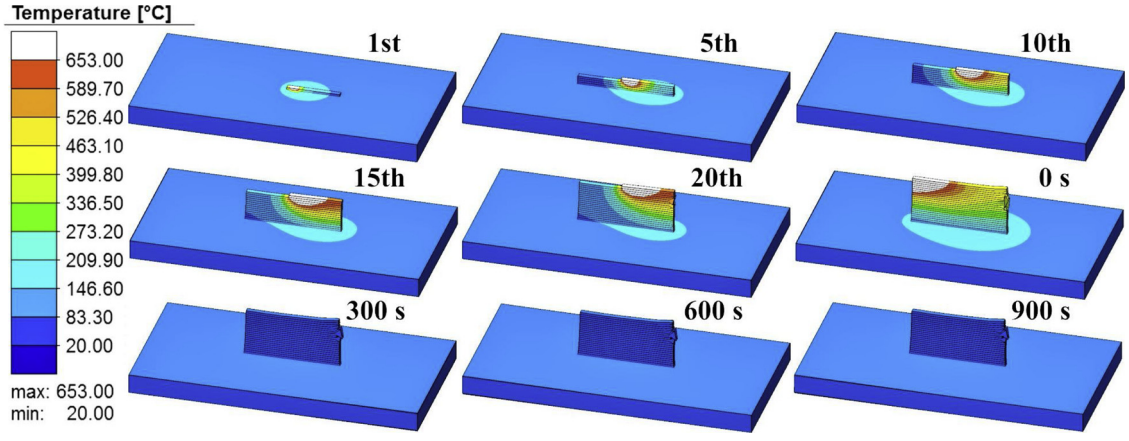

Fig. 17. Temperature field of case 3 during deposition and cooling phase.

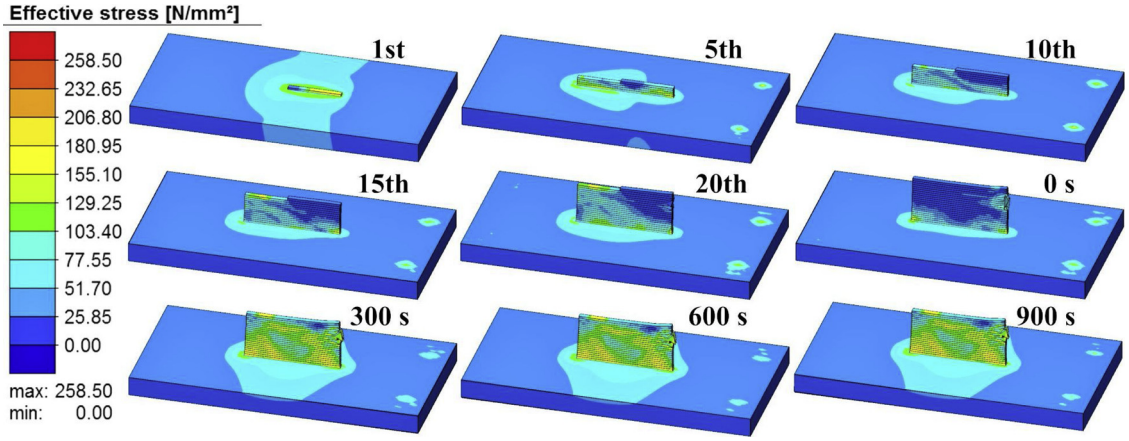

Fig. 18. Distribution of the effective stresses during deposition and cooling phase.

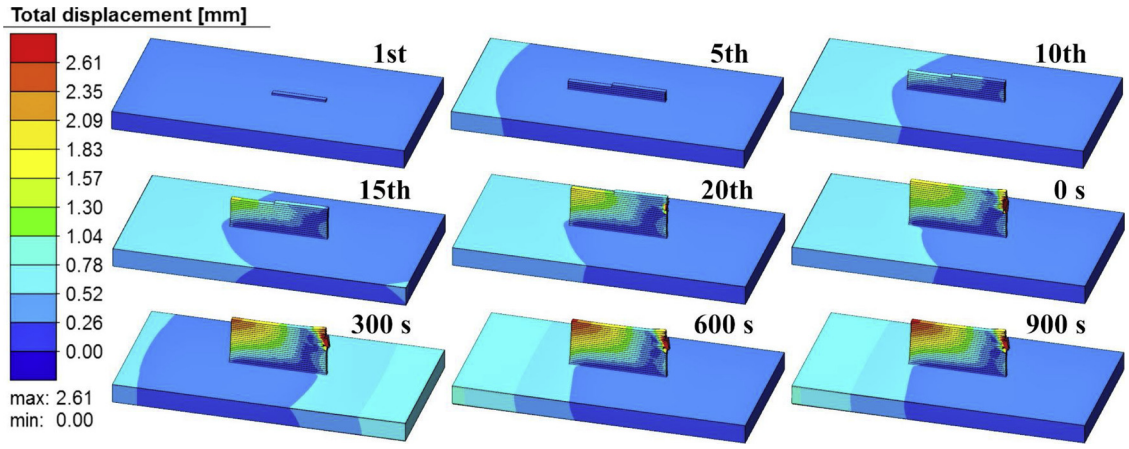

Fig. 19. Total displacement (distortion maxima on three principal axes) field during deposition and cooling phase.

4.3. Residual stress measurements by x-ray

Fig. 21 shows the comparison between the measured and simulated residual stresses at the points presented in Fig. 2, on the surface region of the wall structure. The simulation values were adapted from case 2 and case 3 results and plotted as a function of the distance from the substrate. The measured stress orientation vector is shown in Fig. 2. The chosen simulation cases are among the ones, which were given a 120-seconds time between each deposition layer, imitating the experimental conditions. The stresses were acquired from the surface nodes of the meshed wall geometry from the modelling results to comply with the XRD limitation. The diffracted x-rays originate from an average depth of a few tens of microns from the outermost volume of the material, which is regarded as averaged data from near-surface region of the wall structure. The experimental errors in the x-ray measurements are all well below 10 MPa and therefore, the error bars were not reported. Moreover, due to geometrical constraints in positioning the XRD probe on the sample, only the residual stresses along the deposition direction (S_{11}) was measured.

The simulated stress principal stress values in the x-direction (S_{11}) for case 2 and case 3 on the wall edge are quite comparable. The tensile (positive) stress increase as the measuring points get distant from the

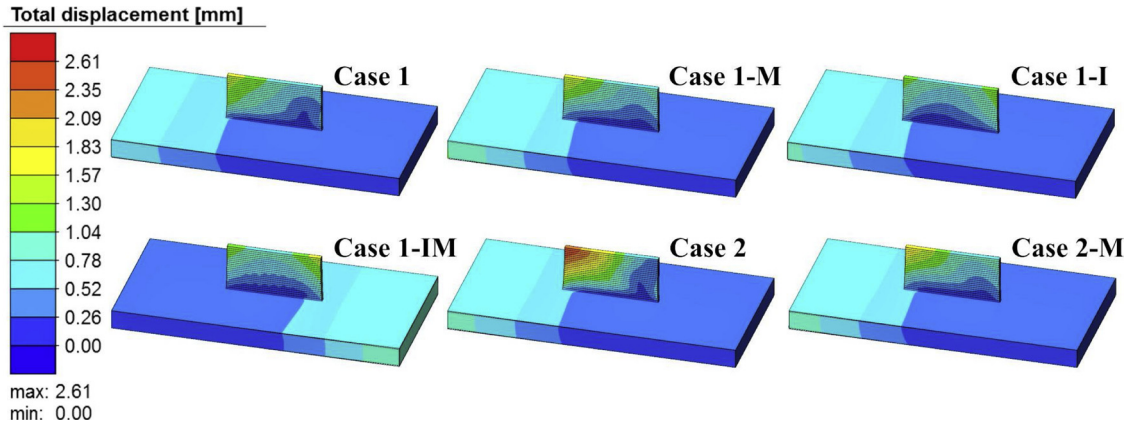

Fig. 20. Comparison of total displacement comparing deposition strategies and materials effect.

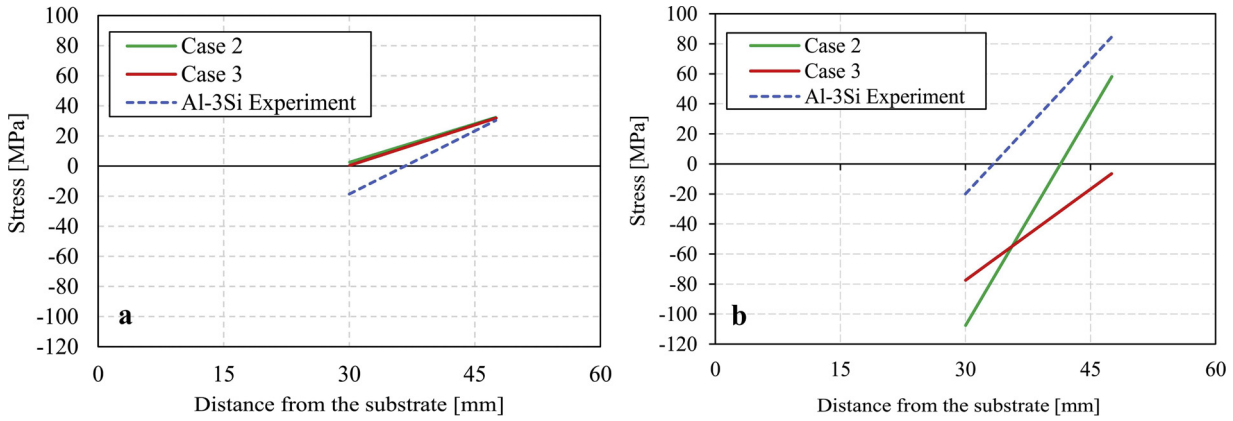

Fig. 21. Horizontal residual stress of wall (a) edge and (b) middle.

substrate in the chosen measurement points. The experimental curve for Al-3Si shows the same trend and almost identical value on the upper point. However, on the lower point, the measured value is on the compressive side.

The numerically determined values for the middle of the wall are different for the two materials. Case 2 that encounters less deformation in the structure, demonstrated higher tensile residual stress on the upper point and higher compressive stress on the lower measurement points. Although the trend from lower to upper points are similar between the numerical and experimental analyses, the values are somewhat contrasting. Case 3 shows all compressive while experimental values from the same material shows mostly tensile stresses. Due to sagging and local deformations, the solidification and heat dissipation conditions will differ for this material and therefore, the experimental results may deviate from the numerically determined values. Moreover, because of the same geometrical deviations, picking the measurement points and transposing their exact location on the modelled wall was challenging. Getting access to the wall middle position for the x-ray probe was rather impractical and therefore, the material was cut close to the middle, still far away from the measurement points. Despite having acceptable distance between the cutting plane and the measurement points, the state of the stresses could be modified once half of the structure was slashed. Another justification for the deviation is indeed implementation of ideal conditions in the model, that might be implausible in the experimental stage. Boundary conditions such as clamping stiffness values in the model can also influence the residual stress results. According to Wang et al. [35], exact clamping positions and the applied forces will bring quite different stress distributions about on the substrate in WAAM processing and in some cases, this will even propagate to the deposited structure.

Regardless of the presented deviation in the residual stress measurement, the modelling approach can still be used for benchmarking and parametric calibration studies, similar to the presented approach for heat source modification.

4.4. Cross-comparison of the cases

Table 6 shows the simulated values of maximum principal stress, distortion and deposition duration for each studied case. The values are colour coded based on the values for each parameter for sake of cross-comparison. The deposition duration of the cases 1, 1-M, 1-I and 1-IM are identical and the lowest compared to the remaining cases. This is due to the fact that there is no idle time between two adjacent layers. For this geometry, introducing the idle time of 120 s results in almost 10 times longer deposition duration, corresponding to 10 times less productivity. The productivity and deposition duration are directly dependent on the length of each layer. The shorter the length of the wall, the more significant the effect of idle time on the productivity.

Among the productive cases, case 1-M show the highest maximum principal stress and distortion. Although the modified heat source parameters are suggested to improve the productivity, it may have negative effect on the evolution of residual stresses and distortion, at least for the given wall structure. This is indeed because of the overall colder process as a result of gradually reduced heat input. Lower heat input at the top layers limits cyclic heat treatment and stress relief on the previously deposited layers. Thus, the residual stresses on each layer contributes to the relatively high maximum principal stress and distortion throughout the entire wall structure.

Case 1I and 1-IM show the lowest maximum principal stress and distortion respectively. When interlaced tool path is selected, the heat source dwells longer on both ends of the wall and therefore, the heat input is somewhat higher at the turning points. This shows that the deposition end points are the regions where the highest stress evolves. This is also reflected in Fig. 19(b) that shows lower residual stress in the middle of the wall compared to the top sides of the wall.

Cases 2 and 2-M are not only less productive but also show relatively high principal stress and distortion values. Like the case 1-M, the total heat input is lower in these cases.

Case 3 shows values in a broad range. The productivity of this case is the lowest since the travel speed of the deposition tool is also slower in addition to the idle time. Because of the lower flow stress of the Al-1Si material at higher temperatures, a few initial layers that cool relatively faster due to heat dissipation to the base plate will cause evolution of low principal stress and distortion. On the top layers, accumulated heat results in evolution of excessive stress and distortion, as indicated by the numbers at the higher bound of the range. For this case, modifying the heat source will be necessary.

Table 6
Maximum stress, distortion and deposition duration of each selected case.

	1	1-M	1-I	1-IM	2	2-M	3
Max. principal stress [MPa]	129.8	140.3	127.3	138	130.2	130.6	24-205
Max. distortion [μm]	263	379	302	51	348	362	1.4-25e3
Deposition duration [s]	275	275	275	275	2795	2795	2887

5. Conclusions

The performed modelling suggests that processing of Al alloys with short intervals and with adaptive heat source modification for each layer are the most effective way to limit the metrological deviations. In addition, the choice of deposition direction will strongly depend on the material flow properties. In general, setting proper boundary conditions is important to acquire results close to a real process. Based on the modelling and computational results, the following conclusions can be drawn:

- Setting heat source modification for every layer is an effective way to conduct WAAM properly and improve deposition efficiency and manufacturability.
- Interval durations in WAAM process should be as short as possible to limit the structural distortion in the aluminium alloys used in this study. This can be interpreted from the total distortion of the deposited wall structure.
- In continuous deposition with interlacing deposition path, the heat source stays longer on the edges of the wall structure (outbound and inbound moves). Even though reversing the deposition direction at every layer makes intervals shorter, it should be performed with extra caution when the material is easy to flow at high temperatures.
- Modelled and measured residual stress on the wall show the same trends from geometrical perspective, yet, somewhat dissimilar values. The boundary conditions and probably the material model for the deposited structure should be fine-tuned for better calculation of residual stresses. The numerical calculations can still be an efficient tool for benchmarking purposes.

Declarations of interest

None.

Acknowledgements

The fund of this work was provided by the AddMan-Al project under the Hydrosfond funding scheme. The authors would like to acknowledge the member of the Hydrosfond board for their support. Mr. Aage Torvund from SimEvolution AS is greatly acknowledged for granting us access to the FE simulation software. Prof. Sigmund Kyrre Ås at Norwegian University of Science and Technology (NTNU), Nina Langhelle and Kenneth Njuolla at SINTEF Ocean are kindly acknowledged for their support in x-ray residual stress measurements.

References

[1] W.E. Frazier, Metal additive manufacturing: a review, J. Mater. Eng. Perform. 23 (6) (2014) 1917–1928.
[2] S.W. Williams, F. Martina, A.C. Addison, J. Ding, G. Pardal, P. Colegrove, Wire+ arc additive manufacturing, Mater. Sci. Technol. Lond. 32 (7) (2016) 641–647.
[3] P. Colegrove, S. Williams, High Deposition Rate High Quality Metal Additive Manufacture Using Wire+ Arc Technology, Cranfield University, 2013.
[4] D. Ding, Z. Pan, D. Cuiuri, H. Li, Wire-feed additive manufacturing of metal components: technologies, developments and future interests, Int. J. Adv. Manuf. Technol. 81 (1-4) (2015) 465–481.
[5] P. Colegrove, A. McAndrew, J. Ding, F. Martina, P. Kurzynski, S. Williams, System architectures for large scale wire+ arc additive manufacture, 10th International Conference on Trends in Welding Research (2016).
[6] S. David, T. DebRoy, Current issues and problems in welding science, Science 257 (5069) (1992) 497–502.
[7] M. Schörghuber, Cold-metal-transfer welding process and welding installation, Google Patents, 2015.
[8] A.S. Azar, A heat source model for cold metal transfer (CMT) welding, J. Therm. Anal. Calorim. 122 (2) (2015) 741–746.
[9] C. Pickin, K. Young, Evaluation of cold metal transfer (CMT) process for welding aluminium alloy, Sci. Technol. Weld. 11 (5) (2006) 583–585.
[10] C.G. Pickin, S.W. Williams, M. Lunt, Characterisation of the cold metal transfer (CMT) process and its application for low dilution cladding, J. Mater. Process. Technol. 211 (3) (2011) 496–502.
[11] B. Cong, J. Ding, S. Williams, Effect of arc mode in cold metal transfer process on porosity of additively manufactured Al-6.3% Cu alloy, Int. J. Adv. Manuf. Technol. 76 (9-12) (2015) 1593–1606.
[12] G. Çam, G. İpekoğlu, Recent developments in joining of aluminum alloys, Int. J. Adv. Manuf. Technol. 91 (5-8) (2017) 1851–1866.
[13] E.P. Zapico, A.H. Lutey, A. Ascari, C.R.G. Pérez, E. Liverani, A. Fortunato, An improved model for cold metal transfer welding of aluminium alloys, J. Therm. Anal. Calorim. 131 (3) (2018) 3003–3009.
[14] P. Almeida, S. Williams, Innovative process model of Ti–6Al–4V additive layer manufacturing using cold metal transfer (CMT), Proceedings of the Twenty-First Annual International Solid Freeform Fabrication Symposium (2010).
[15] C. Zhang, Y. Li, M. Gao, X. Zeng, Wire arc additive manufacturing of Al-6Mg alloy using variable polarity cold metal transfer arc as power source, Mater. Sci. Eng. A 711 (2018) 415–423.
[16] A. Horgar, H. Fostervoll, B. Nyhus, X. Ren, M. Eriksson, O. Akselsen, Additive manufacturing using WAAM with AA5183 wire, J. Mater. Process. Technol. 259 (2018) 68–74.
[17] X. Fang, L. Zhang, H. Li, C. Li, K. Huang, B. Lu, Microstructure evolution and mechanical behavior of 2219 aluminum alloys additively fabricated by the cold metal transfer process, Materials 11 (5) (2018) 812.
[18] E. Ryan, T. Sabin, J. Watts, M. Whiting, The influence of build parameters and wire batch on porosity of wire and arc additive manufactured aluminium alloy 2319, J. Mater. Process. Technol. (2018).
[19] Y. Nie, P. Zhang, X. Wu, G. Li, H. Yan, Z. Yu, Rapid prototyping of 4043 Al-alloy parts by cold metal transfer, Sci. Technol. Weld. (2018) 1–9.
[20] S. Hu, H. Zhang, Z. Wang, Y. Liang, Y. Liu, The arc characteristics of cold metal transfer welding with AZ31 magnesium alloy wire, J. Manuf. Process. 24 (2016) 298–306.
[21] N. Sridharan, M.W. Noakes, A. Nycz, L.J. Love, R.R. Dehoff, S.S. Babu, On the toughness scatter in low alloy C-Mn steel samples fabricated using wire arc additive manufacturing, Mater. Sci. Eng. A 713 (2018) 18–27.
[22] J. Ge, J. Lin, Y. Lei, H. Fu, Location-related thermal history, microstructure, and mechanical properties of arc additively manufactured 2Cr13 steel using cold metal transfer welding, Mater. Sci. Eng. A 715 (2018) 144–153.
[23] N. Rodriguez, L. Vázquez, I. Huarte, E. Arruti, I. Tabernero, P. Alvarez, Wire and arc additive manufacturing: a comparison between CMT and TopTIG processes applied to stainless steel, Weld World (2018) 1–14.
[24] J. Ding, Thermo-mechanical Analysis of Wire and Arc Additive Manufacturing Process, (2012).
[25] J. Ding, P. Colegrove, J. Mehnen, S. Ganguly, P.S. Almeida, F. Wang, S. Williams, Thermo-mechanical analysis of wire and arc additive layer manufacturing process on large multi-layer parts, Comput. Mater. Sci. 50 (12) (2011) 3315–3322.
[26] E.R. Denlinger, J. Irwin, P. Michaleris, Thermomechanical modeling of additive manufacturing large parts, J. Manuf. Sci. Eng. 136 (6) (2014) 061007.
[27] F. Montevecchi, G. Venturini, A. Scippa, G. Campatelli, Finite element modelling of wire-arc-additive-manufacturing process, Proc. Cirp 55 (2016) 109–114.
[28] S. Boschert, R. Rosen, Digital Twin—the Simulation Aspect, Mechatronic Futures, Springer, 2016, pp. 59–74.
[29] G. Knapp, T. Mukherjee, J. Zuback, H. Wei, T. Palmer, A. De, T. DebRoy, Building blocks for a digital twin of additive manufacturing, Acta Mater. 135 (2017) 390–399.
[30] M. Fitzpatrick, A. Fry, P. Holdway, F. Kandil, J. Shackleton, L. Suominen, Determination of Residual Stresses by X-ray Diffraction, (2005).
[31] J. Goldak, A. Chakravarti, M. Bibby, A new finite element model for welding heat sources, Metall. Trans. B 15 (2) (1984) 299–305.
[32] A.S. Azar, S.K. As, O.M. Akselsen, Determination of welding heat source parameters from actual bead shape, Comput. Mater. Sci. 54 (2012) 176–182.
[33] F. Montevecchi, G. Venturini, N. Grossi, A. Scippa, G. Campatelli, Idle time selection for wire-arc additive manufacturing: a finite element-based technique, Addit. Manuf. 21 (2018) 479–486.
[34] G. Zhu, D. Li, A. Zhang, G. Pi, Y. Tang, The influence of standoff variations on the forming accuracy in laser direct metal deposition, Rapid Prototyp. J. 17 (2) (2011) 98–106.
[35] X. Wang, A. Wang, Finite element analysis of clamping form in wire and arc additive manufacturing, modeling, simulation, and applied optimization (ICMSAO), 2017 7th International Conference on IEEE, (2017), pp. 1–5.